
STOCHASTIC HIERARCHICAL DATA-DRIVEN OPTIMIZATION: APPLICATION TO PLASMA-SURFACE KINETICS

José Afonso¹, Vasco Guerra¹, and Pedro Viegas^{*1}

¹Instituto de Plasmas e Fusão Nuclear, Instituto Superior Técnico, Av. Rovisco Pais 1, Lisbon, Portugal

ABSTRACT

This work introduces a stochastic hierarchical optimization framework inspired by Sloppy Model theory for the efficient calibration of physical models. Central to this method is the use of a reduced Hessian approximation, which identifies and targets the stiff parameter subspace using minimal simulation queries. This strategy enables efficient navigation of highly anisotropic landscapes, avoiding the computational burden of exhaustive sampling. To ensure rigorous inference, we integrate this approach with a probabilistic formulation that derives a principled objective loss function directly from observed data. We validate the framework by applying it to the problem of plasma-surface interactions, where accurate modelling is strictly limited by uncertainties in surface reactivity parameters and the computational cost of kinetic simulations. Comparative analysis demonstrates that our method consistently outperforms baseline optimization techniques in sample efficiency. This approach offers a general and scalable tool for optimizing models of complex reaction systems, ranging from plasma chemistry to biochemical networks.

Keywords Plasmas Kinetic Scheme · Hierarchical Optimization · Inverse Problem

1 Introduction

The predictive modeling of complex natural systems, ranging from biochemical networks [1] and chemical engineering to plasma physics, often relies on multiphysics simulations constrained by numerous free parameters. A prevalent feature of these systems is their *sloppy* nature [2, 3]: while the model may possess high-dimensional parameter spaces, its relevant physical behavior typically evolves along a low-dimensional latent manifold [4]. This observation aligns with the *manifold hypothesis* in Scientific Machine Learning [5], which posits that meaningful signal can be separated from unidentifiable degrees of freedom by identifying the system’s intrinsic geometry. Consequently, the refinement of these scientific models constitutes a challenging, ill-conditioned inverse problem where determining physical parameters from limited data is hindered by the ruggedness of the optimization landscape and the computational cost of the simulator.

Optimization techniques for such problems generally follow one of two strategies regarding their use of statistical approximations. The first strategy aims to improve sample efficiency by constructing a global statistical surrogate (e.g., Gaussian Processes) of the objective function [6–8]. This allows the optimization to proceed on a computationally cheap proxy rather than the expensive simulator. However, relying on a surrogate introduces the risk that the optimization process could be misguided towards a false minimum that exists on the proxy’s response surface but not in the true physical landscape.

The alternative strategy is to query the simulator directly, treating it as the ground truth without attempting to fit a global statistical proxy [6]. In this work, we opt for this direct approach, motivated by the manageable computational cost of many simulators [9]. In this intermediate regime, while exhaustive sampling remains prohibitive, the trade-off of accepting the approximation error of a statistical surrogate is often unjustified. Instead, the challenge shifts to prioritizing sample efficiency: finding the optimal fit with the minimum number of simulator queries. This focus is critical to ensure the framework’s scalability to more complex models, where a single evaluation may be significantly

^{*}Corresponding author: pedro.a.viegas@tecnico.ulisboa.pt

more expensive. Additionally, a major hurdle to efficiency is that these simulators often provide neither analytical nor numerical gradients.

To achieve sample efficiency without surrogates, we operationalize the manifold hypothesis by exploring the synergies between physical modeling and representation learning [2, 10]. Rather than performing a blind search, we frame the optimization as a geometric inference task: separating meaningful signals from unidentifiable degrees of freedom. This reasoning parallels the logic of data-driven autoencoders, where the objective is to learn a compressed representation that captures the dominant features of the system [11]. Crucially, explicitly targeting this latent structure addresses the severe low-data regime inherent to computationally expensive simulators; by distinguishing the essential determinants from irrelevant parameters, we can achieve inference with a fraction of the samples required by standard *black-box* methods.

We implement this conceptual framework by leveraging the specific geometric structure of the residuals. We adopt a *stochastic hierarchical* optimization algorithm informed by Sloppy Model theory [12] that utilizes a reduced Hessian strategy. This operator functions as a linear autoencoder for the local landscape, efficiently identifying the *stiff* (physically meaningful) parameter directions using minimal simulator queries. Furthermore, to ensure rigorous parameter inference in the presence of experimental and model errors, we construct the loss landscape using a principled probabilistic objective function. This formulation, derived from maximum likelihood estimation, explicitly accounts for uncertainties in the macroscopic observables, providing a robust metric for model optimization.

We demonstrate the efficacy of this framework in the field of plasma-surface interactions, a domain where these optimization challenges are particularly acute. The accurate description of plasma kinetics is essential to applications ranging from material processing [13] and sustainable plasma catalysis [14] to fusion energy [15]. However, the models describing these phenomena require surface reactivity parameters (e.g., sticking coefficients, energy barriers) that are often poorly defined or unknown [16–18]. Calibrating these parameters is critical, yet the simulations are computationally expensive, rendering naive global search methods infeasible.

The specific case study addressed in this work is a mesoscopic surface kinetics model describing the recombination of atomic oxygen on a Pyrex wall in O_2/CO_2 glow discharge reactors, based on the framework established in [16–20]. To ensure a robust refinement, we utilize a comprehensive dataset comprising 225 distinct steady-state conditions compiled from the literature [18–20]. These experiments cover a wide operational space, including pressures from 0.2 to 10 Torr, discharge currents between 10 and 40 mA, and wall temperatures from $-20^\circ C$ to $50^\circ C$.

To benchmark the performance of the proposed hierarchical approach, we compare it against five baseline algorithms selected to isolate different optimization challenges: Differential Evolution (DE) [21] for global exploration; Covariance Matrix Adaptation Evolution Strategy (CMA-ES) [22] for adaptation to ill-conditioned landscapes; Trust Region Reflective (TRF) [23] and Powell’s method [24] for local refinement; and Gaussian Processes (GP) [25] to evaluate the efficacy of statistical surrogate modeling.

The remainder of the paper is organized as follows: Section 2 presents the probabilistic problem formulation and the hierarchical algorithms explored. Section 3 details the experimental dataset and the physical description of the simulator model. Section 4 presents the results of applying the proposed methods to the O_2 and CO_2 plasma-surface kinetics schemes. Finally, Section 5 discusses our findings and presents the conclusions.

2 Methods

2.1 Problem Formulation

The foundation of the model is a surface kinetics scheme that describes the elementary processes occurring at the interface between a low-temperature plasma and a Pyrex (borosilicate glass) surface [16–18]. This scheme is translated into a system of coupled Ordinary Differential Equations (ODEs) that governs the temporal evolution of the chemical species’ densities. The solution of this system depends on a vector of n kinetic parameters, $\theta \in \mathbb{R}^n$, which includes terms such as energy barriers and steric factors of the reaction rate coefficients [16].

For a given set of parameters θ , the system of ODEs is numerically integrated until an arbitrary time τ is reached. In this work, τ is assumed to be the duration required for the system to achieve stationarity. From this τ state, a vector of m macroscopic observables, $M(\theta) \in \mathbb{R}^m$, is computed. These observables may include quantities such as surface recombination probabilities [16, 18], surface coverages, or gas species densities, which are directly compared to a set of experimental measurements, denoted by the vector $E \in \mathbb{R}^m$. Hence, the problem is framed as an optimization exercise where the goal is to minimize the objective function:

$$\theta^* = \arg \min_{\theta \in \Theta} \Phi(\theta), \quad (1)$$

where $\Theta \subseteq \mathbb{R}^n$ is the domain of physically admissible parameter vectors (i.e., the set of all parameter vectors that satisfy the imposed physical constraints and limits), and $\Phi : \Theta \rightarrow \mathbb{R}_{\geq 0}$ is the objective loss given by:

$$\Phi(\theta) = \frac{1}{2} \sum_{i \in \mathcal{D}} \sum_{j=1}^m \left(r_j^{(i)}(\theta) \right)^2, \quad r_j^{(i)}(\theta) = \frac{E_j^{(i)} - M_j^{(i)}(\theta)}{E_j^{(i)}}, \quad (2)$$

where we assume that the experimental measurements are independent and normally distributed. Moreover, \mathcal{D} corresponds to the experimental dataset, and r represents the residuals. The full derivation of the objective function from the probabilistic framework is detailed in Appendix A.

2.2 Baseline Optimization Algorithms

We select five baseline algorithms, each representing a different strategy in non-linear least-squares optimization. These methods allow us to evaluate separately the challenges of global exploration, landscape adaptation, gradient estimation, local refinement, and surrogate modeling.

As a baseline for global exploration, we employ Differential Evolution (DE), a population-based heuristic method [21]. While effective at surveying the entire parameter space to avoid local minima, its performance is significantly hindered by the objective function's ill-conditioning, a well-known difficulty for the general class of sloppy models [12] that we also analyze for our model in Section 4. DE's use of isotropic search strategies struggles to make progress in landscapes with vastly different parameter sensitivities.

To specifically address the ill-conditioning difficulty, we use the Covariance Matrix Adaptation Evolution Strategy (CMA-ES) as an adaptive baseline [22]. This method is more suited for the narrow, elongated valleys of our problem, as it learns the landscape's geometry by adapting its internal covariance matrix.

To benchmark standard local refinement strategies, we employ two distinct approaches. First, we include the Trust Region Reflective (TRF) algorithm [23], a robust bound-constrained extension of the classic Levenberg-Marquardt method [26], in which the Jacobian matrix is estimated via finite differences. Second, we include Powell's method, a classic non-population-based algorithm [24]. Unlike TRF, it operates by performing iterative line searches along a set of optimized directions without requiring any gradient estimation.

While our primary focus remains on methods that query the simulator directly, we also explore a widely used surrogate-based method, Gaussian Process (GP), for completeness [25]. The implementation details of the baseline algorithms are presented in the Appendix B.

2.3 Hierarchical Optimization

Building on the insights that our loss $\Phi(\theta)$ is ill-conditioned and the difficulties found when exploring the baseline methods, we adopt an adaptive strategy that leverages the problem's geometric structure. Informed by Sloppy Model theory [2, 4, 12, 27], we reframe the search for a minimum as an iterative process guided by a geometric heuristic space partition [28] that starts from a given initial parameter guess $\theta^{(0)}$. The scheme 1 presents a schematic overview of the algorithm considered.

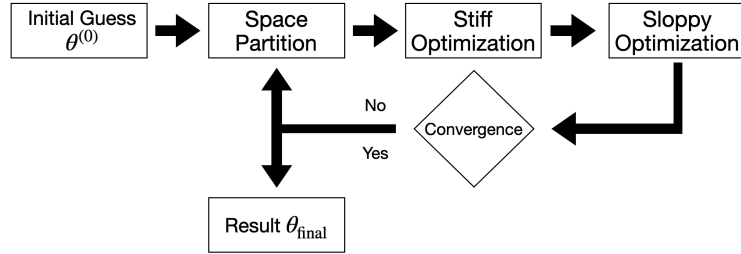


Figure 1: Hierarchical algorithm overview diagram

2.3.1 Geometric Model Injection via the Gauss-Newton Hessian

The heart of the heuristic space partition is a local model of the objective loss function Φ that explicitly takes into account the fact that the objective loss is dominated by a set of *stiff* directions, while the remaining *sloppy* modes contribute negligibly [4, 12, 27]. This decomposition is based on the information provided by the Hessian matrix of the

objective loss. Under the assumption that the residuals, r (Eq.(2)), are small, the objective loss' Hessian of the estimate at iteration i , $\theta^{(i)}$, is well approximated by

$$[H(\theta^{(i)})]_{mn} = [\nabla^2 \Phi(\theta^{(i)})]_{mn} \approx [H_{\text{GN}}(\theta^{(i)})]_{mn} = \sum_l \frac{\partial r_l}{\partial \theta_m} \frac{\partial r_l}{\partial \theta_n}, \quad (3)$$

where H_{GN} corresponds to the *Gauss-Newton* approximation of the Hessian matrix [29]. The eigendecomposition of this matrix,

$$H_{\text{GN}}(\theta^{(i)}) = V \Lambda V^T, \quad \Lambda = \text{diag}(\lambda_1, \dots, \lambda_n), \quad (4)$$

reveals a near-universal property of these models [2, 12]. As we will see in Fig. 2(d), the eigenvalue spectrum $\{\lambda_i\}$ decays exponentially, exposing a small set of *stiff* parameter combinations that dominate the model's behavior and a large set of *sloppy* combinations that have a negligible effect. This justifies the hierarchical optimization approach. We partition the eigenpairs $\{(\lambda_i, v_i)\}$ of H_{GN} , where v_i are the eigenvectors, into two different subspaces. The stiff subspace $V_s = \text{span}\{v_1, v_2, \dots, v_k\}$ is spanned by the eigenvectors corresponding to the large eigenvalues (λ_i) , while the *sloppy* subspace, V_l , is its orthogonal complement. The splitting criteria is based on the cumulative variance conveyed by the eigenspectrum, analogous to Principal Component Analysis (PCA) [30] (see Appendix C for details on the λ_i and the subspace definitions).

Any parameter vector, $\theta \in \mathbb{R}^n$, can be expressed as a deviation from $\theta^{(i)}$ along the natural coordinates defined by the eigenspace of $H_{\text{GN}}(\theta^{(i)})$:

$$\theta = \theta^{(i)} + V_s^{(i)}\phi + V_l^{(i)}\psi. \quad (5)$$

where $\phi \in \mathbb{R}^k$ and $\psi \in \mathbb{R}^{n-k}$ are the coordinate vectors representing the deviation within the stiff and sloppy subspaces, respectively.

Moreover, we further improve the sample efficiency in our optimization problem by reducing the dimensionality of the input space. By analyzing the eigenspectrum of H_{GN} , we remove less significant dimensions, creating a *reduced* sloppy subspace that focuses on its most important directions. Although this sacrifices a complete basis for the new coordinate system, our algorithm's iterative nature helps to mitigate this issue (see Appendix C for more details).

2.3.2 Implicit Curvature via the Reduced Hessian Proxy

While the full eigendecomposition (Eq. 4) provides a complete map of the landscape, constructing the full Gauss-Newton Hessian requires computing the full matrix $J_{mn} = \partial r_m / \partial \theta_n$. When the underlying simulator is computationally expensive, performing $n + 1$ simulator evaluations to build J becomes intractable for high-dimensional parameter spaces.

To circumvent this limitation, we employ a reduced Hessian strategy that acts as an efficient proxy to identify the stiff subspace. This approach can be viewed as a *linear autoencoder* for the local curvature [12]. Just as an autoencoder compresses data into a latent space to preserve the most significant features, we restrict our curvature search to a lower-dimensional random subspace $\Omega \in \mathbb{R}^{n \times k}$ (with subspace dimension $k \ll n$) to capture the maximum *stiffness* energy [31].

Mathematically, maximizing the curvature within this subspace (defined by the Rayleigh Quotient [32]) is equivalent to analyzing the eigenvalues of the reduced matrix H_{small} :

$$H_{\text{small}} = \Omega^T H_{\text{GN}} \Omega = (J\Omega)^T (J\Omega). \quad (6)$$

This formulation allows us to compute the dominant curvature implicitly. By defining $Y = J\Omega$, we can approximate the columns of Y directly via finite differences along the basis directions Ω [33] (see Appendix D for the derivation). This reduces the computational cost from $n + 1$ simulator calls to just $k + 1$ calls, making it feasible to extract the stiff geometry even for expensive simulators.

The success of this approximation relies on the specific geometry of sloppy models. Provided the stiffness ratio (the gap between λ_{stiff} and λ_{sloppy}) is sufficiently large, the energy landscape inside the random subspace is dominated by the projection of the true stiff modes [4]. Solving the eigenvalue problem for H_{small} yields the optimal rotation of our random basis, providing the approximate stiff basis V_s required for the update rule in Eq. (3) (see Appendix E for the derivation).

2.3.3 Heuristic Meta-Simulator (\mathcal{H})

The space decomposition allows us to replace the original, intractable joint optimization with a more manageable, sequential one. We formalize this step as the application of the *heuristic meta-simulator* operator, \mathcal{H}_i , where index i

signals that the operator is applied to the given estimate at iteration i , $\theta^{(i)}$. This operator maps the parameter vector $\theta^{(i)}$ to the next, $\theta^{(i+1)}$, by executing a search constrained by the geometric model derived at $\theta^{(i)}$. The operation $\theta^{(i+1)} = \mathcal{H}_i(\theta^{(i)})$ is a composition of three sequential subproblems:

- Stiff optimization: We minimize the stiff space defined by V_s :

$$\theta^{(i')} = \theta^{(i)} + V_s^{(i)} \phi^*, \quad \text{where } \phi^* = \arg \min_{\phi} \Phi(\theta^{(i)} + V_s^{(i)} \phi) \quad (7)$$

- Sloppy re-alignment: We re-orient the coordinate system to align with the local curvature of the sloppy subspace. We compute a reduced Hessian strictly within the sloppy subspace V_l and solve its eigenproblem to obtain a rotation matrix U :

$$V_l' = V_l U \quad (8)$$

This rotation decorrelates the parameters, ensuring that the subsequent optimizer moves along the valley's principal axes rather than traversing diagonally across ridges [4].

- Sloppy optimization: We perform search along V_l' :

$$\theta^{(i+1)} = \theta^{(i')} + V_l'^{(i)} \psi^*, \quad \text{where } \psi^* = \arg \min_{\psi} \Phi(\theta^{(i')} + V_l'^{(i)} \psi) \quad (9)$$

This sequential procedure constitutes a single step guided by the local geometry of the manifold.

2.3.4 Iterative Refinement via Space Update

A static model based on the geometry at $\theta^{(i)}$ is insufficient to navigate the objective surface Φ . The key to the method's power is the *iterative refinement* of the heuristic operator \mathcal{H}_i in the style of *Manifold Boundary Approximation Method* [28]. After each step, the old operator \mathcal{H}_i and its underlying basis V_i are discarded. A new heuristic operator \mathcal{H}_{i+1} is then constructed by re-evaluating the geometry on the new point $\theta^{(i+1)}$. Hence, the overall optimization at the iteration i , $\theta^{(i)}$, is a sequence of applications of these adaptive operators that starts from the initial guess $\theta^{(0)}$:

$$\theta^{(i)} = (\mathcal{H}_{i-1} \circ \dots \circ \mathcal{H}_0)(\theta^{(0)}), \quad (10)$$

where \circ denotes the composition operator.

This iterative process allows the algorithm to *see* the changing landscape and adjust the coordinate system, enabling it to follow the curved, *narrow valleys* characteristics of the *sloppy* model. The formal description of the algorithm is presented in Appendices B and C.

2.3.5 Convergence and region of near-optimal parameters

The algorithm guarantees reaching a stationary point. Indeed, since each subproblem is solved by a descent method, the objective function is guaranteed to be non-increasing: $\Phi(\theta^{(i+1)}) \leq \Phi(\theta^{(i)})$. Moreover, as $\Phi > 0$, the sequence must converge.

As termination criteria, we consider the stability of the *stiff* subspace [28]. Convergence of the algorithm is assumed when the stiff subspace stops rotating, which is measured by analyzing the singular values $\{\sigma_j\}$ of the singular value decomposition of the overlap matrix $V_s^{(i+1),T} V_s^{(i)}$. The misalignment, $\delta_s = \max_j (1 - \sigma_j)$, indicates convergence when it falls below a tolerance, $\delta_s < \varepsilon_{\text{stop}}$.

The criterion ensures the converged point, θ_{final} , has *almost* the properties of a true minimum, as it is ensured that the final gradient lies in the *sloppy* subspace, which implies that the l_2 -norm of the gradient is bounded:

$$\|\nabla \Phi(\theta_{\text{final}})\|_2 \leq |\lambda_{\max \text{ sloppy}}| \cdot \|\Delta \theta\|_2. \quad (11)$$

where $\Delta \theta$ is the difference between θ_{final} (the algorithm's estimation at the last iteration) and the true local minimum θ_{\min} . Appendix F presents the full derivation of Eq.(11). Since $\lambda_{\max \text{ sloppy}}$, the largest eigenvalue (in magnitude) of the *sloppy* space is small ($\lambda_{\max \text{ sloppy}} / \lambda_{\max \text{ stiff}} \ll 1$), the norm of the gradient at the converged point is guaranteed to be small.

The algorithm is formally a local method and does not guarantee finding the global minimum, θ_{global} . However, this procedure is often sufficient for sloppy models, where the set of near-optimal parameters, $\mathcal{S}_\epsilon = \{\theta \in \mathbb{R}^n \mid \Phi(\theta) \leq \Phi(\theta_{\text{global}}) + \epsilon\}$ with $\epsilon > 0$, is typically a large, high-dimensional, and extended region in the parameter space [4, 12, 27].

The reason for the sloppy structure can be understood by analyzing the geometry of the loss function Φ around a found minimum, θ_{\min} . The Hessian evaluated at this point, $H \equiv H(\theta_{\min})$, which has eigenvectors $\{v_i\}$ and eigenvalues $\{\lambda_i\}$. The change in the loss function, $\Delta\Phi$, for small deviation $\Delta\theta$ is given by the quadratic approximation:

$$\Delta\Phi \approx \frac{1}{2} \Delta\theta^T H \Delta\theta. \quad (12)$$

Assuming that deviations $\Delta\theta$ lie solely within the sloppy subspace, which is spanned by the eigenvectors $\{v_j\}_{j \in \text{sloppy}}$, the deviations can be written as $\Delta\theta = \sum_{j \in \text{sloppy}} \alpha_j v_j$. Replacing this in the quadratic approximation gives:

$$\Delta\Phi \approx \frac{1}{2} \left(\sum_{i \in \text{sloppy}} \alpha_i v_i^T \right) H \left(\sum_{k \in \text{sloppy}} \alpha_k v_k \right) \quad (13)$$

By expressing the Hessian in its eigenbasis, $H = \sum_j \lambda_j v_j v_j^T$, and using the orthonormality of the eigenvectors ($v_i^T v_j = \delta_{ij}$), it simplifies to:

$$\Delta\Phi \approx \frac{1}{2} \sum_{j \in \text{sloppy}} \lambda_j \alpha_j^2 \quad (14)$$

Since all sloppy eigenvalues λ_j are small (many orders of magnitude smaller than the stiff eigenvalues), this equation shows that large displacements in parameter space along the sloppy space (large coefficients α_j) produce negligible changes in Φ . This explains the extended region \mathcal{S}_ϵ . Conversely, any deviation along a stiff direction would be heavily penalized by its large eigenvalue, confining the set of good parameters [2].

3 Physical System and Experimental Data

3.1 Simulator's Physical Model: Surface Kinetics on Pyrex

The case study analyzed in this work concerns a mesoscopic surface kinetics model that describes the interaction between an O₂/CO₂ glow discharge and a Pyrex reactor wall. To the best of our knowledge, this formulation represents the current state-of-the-art for describing plasma-surface recombination. The model is developed within the theoretical framework established in earlier studies [16–20], and both encompasses and extends the earlier results from [16–18], which investigated O-atom recombination in O₂ glow discharges, as well as the preliminary findings for CO₂ plasmas reported in [19, 20]. The model accounts for adsorption, surface diffusion, and recombination of key reactive species, including atomic oxygen (O), molecular oxygen (O₂), ozone (O₃), carbon monoxide (CO), and carbon dioxide (CO₂).

The model considers three distinct adsorption sites on the Pyrex surface. Physisorption sites (F_V) cover the entire surface, binding particles through weak, reversible van der Waals forces. Chemisorption sites (S_V), located at surface defects, form strong, irreversible chemical bonds. Additionally, at low pressures (< 1 Torr), ion bombardment can create highly reactive, reversible metastable sites (S_V^{*}). Recombination of atomic species occurs via two main mechanisms: the Eley-Rideal (E-R) mechanism, where the gas-phase particle, A(g), reacts directly with an adsorbed particle A_(F/S) (F in the case of a physisorption site and S for the chemisorption one) $(A(g) + A_{(F/S)} \longrightarrow A_2(g) + (F/S)_V)$ and the Langmuir-Hinshelwood (L-H) mechanism, involving two adsorbed particles $(A_F + A_{(F/S)} \longrightarrow A_2(g) + (F/S)_V + F_V)$. The full reaction scheme comprises 62 elementary reactions and a total of 125 parameters [18, 20]. The oxygen atom kinetics is temperature-dependent: at low pressures ($T_w < 25^\circ\text{C}$), recombination is dominated by reactions like (O_F + O_F \longrightarrow O₂(g) + 2F_V) (L-H), while at higher temperatures ($T_w > 25^\circ\text{C}$), reactions involving chemisorbed oxygen, such as (O(g) + O_S \longrightarrow O₂(g) + S_V) (E-R), become dominant. The inclusion of carbon species is critical for CO₂ plasmas, where the primary effect is the passivation of reactive chemisorption sites by CO, which competes with oxygen and significantly reduces the overall O-atom recombination rate [19, 20, 34]. The net effect of this micro-kinetic scheme is consolidated into a single macroscopic observable M : the effective recombination probability of atomic oxygen, denoted as γ_O . Crucially, while limited to a single scalar, this observable encodes complex dependencies on pressure, discharge current, and gas mixture, measured across 225 different experimental conditions.

3.2 Parameters for Optimization

The predictive accuracy of the kinetic model depends on its rate constants, many of which are not well understood from first principles or experimental data. The goal of this work is to refine a subset of the model parameters, namely the Arrhenius parameters ($k_{0,i}$ and $E_{a,i}$), by fitting the model macroscopic observable γ_O to experimental data. These parameters define the rate coefficients, $k_i = k_{0,i} \cdot \exp(-E_{a,i}/k_B T)$, that are used within the model [16]. The parameters to be optimized are presented in a vector θ , which includes:

- Energy barriers ($E_{a,i}$): the activation energies for the creation and destruction of metastable surface sites (S_V^*)
- Steric Factors ($k_{0,i}$) : The pre-exponential factors for the chemical equations involving CO and the metastable sites.
- Desorption Frequency Parameters: For the desorption of physisorbed species (O_F, O_{2F}, CO_F), the desorption frequency is described by the parameterization $\nu_d(T) = 10^{15} \times (A + B \cdot \exp(E/k_B T)) \text{ s}^{-1}$ [18], where the coefficients A, B , and E are to be optimized.

In total, the optimization problem addresses 29 distinct parameters, which correspond to the ones with the highest uncertainty estimation [18, 20]

3.3 Experimental Validation Dataset

The dataset, compiled from the literature [18] and from unpublished measurements used in [19, 20], provides the γ_O observable across 225 distinct steady-state conditions. These experiments cover a wide operational space, including O_2/CO_2 gas mixtures with a total flow rate of 7.4 sccm, pressures from 0.2 to 10 Torr, discharge currents between 10 and 40 mA, and wall temperatures from -20°C to 50°C .

4 Results

In this section, we evaluate the performance of the proposed hierarchical algorithm against the baseline methods. To address validation concerns and demonstrate predictive capability beyond simple curve fitting, we partition the experimental dataset into a training set (80%, $N = 180$) and a held-out test set (20%, $N = 45$). All optimizations were restricted to the training set, while the test set was used post-optimization to verify the generalization of the found solutions. As required for a fair comparison, all algorithms were initialized with the same parameter guess, $\theta^{(0)}$, which significantly differs from the literature default ($\Phi(\theta^{(0)}) \approx 700$ vs. $\Phi(\theta_{\text{default}}) \approx 0.1$).

Figure 2(a) presents the global convergence of the training loss (Φ_{train}) for all algorithms. Critically, the x-axis represents cumulative simulator calls. Since the kinetic simulation constitutes the dominant computational bottleneck, this axis serves as the direct metric for sample efficiency. The Hierarchical methods, comprising the exact full-Jacobian formulation (red) and the stochastic proxy with $k=18$ (pink), demonstrate superior convergence speed compared to the global (DE, CMA-ES) and gradient-free local (Powell) baselines. While the Trust Region Reflective algorithm (TRF, purple line) proves to be a strong competitor, eventually reaching a similar loss floor, the Hierarchical approach achieves high-quality solutions with significantly fewer iterations in the intermediate regime. This acceleration is driven by the algorithm's ability to exploit the highly anisotropic structure of the loss landscape, rapidly converging onto the low-energy manifold (the valley floor) before refining the sloppy parameters.

Crucially, for computationally expensive simulators, the primary metric of interest is sample efficiency: the ability to find good parameters with minimal model evaluations. Figure 2(b) analyzes this by comparing the *Hierarchical Exact* strategy against the *Hierarchical Stochastic* (reduced Hessian) strategy with varying subspace sizes k . The results reveal a striking advantage for the stochastic approach: even with subspace dimensions as low as $k = 3$ or $k = 5$, a massive compression relative to the full parameter space of $n = 29$, the algorithm achieves a rapid loss reduction in the first 20 iterations, significantly outperforming the Exact method. This confirms that the stiffest features of the landscape can be identified and exploited using only a coarse, low-rank approximation of the curvature, validating the framework's scalability to more complex models where n is large.

To ensure that these optimized parameters correspond to a physically meaningful model rather than an artifact of overfitting, we examine the generalization error in Figure 2(c). Here, we track both the training loss (dotted lines) and test loss (solid lines) throughout the optimization for the top-performing algorithms (TRF and Hierarchical). The close alignment between the training and test trajectories indicates that the algorithms are not overfitting. The Hierarchical method achieves a final test loss comparable to the TRF baseline, confirming that the *sloppy* geometric separation is a robust feature of the physical model that allows for reliable extrapolation to unseen experimental conditions.

Finally, Figure 2(d) displays the eigenvalue spectrum of the Hessian at the found minimum. The rapid decay of eigenvalues (λ_i) spanning several orders of magnitude confirms the underlying sloppy nature of the model, justifying the hierarchical separation of parameter space that drives our algorithm's efficiency.

To assess the robustness of the identified parameters and ensure they represent physical reality rather than statistical artifacts, the optimization was executed using the Hierarchical Exact algorithm, starting from the previous initial guess ($\Phi(\theta^{(0)}) \approx 700$). This procedure was performed independently on five distinct training/test splits (80%/20%), where we employed stratified random sampling based on the joint Pressure-Temperature distribution. This ensures that both

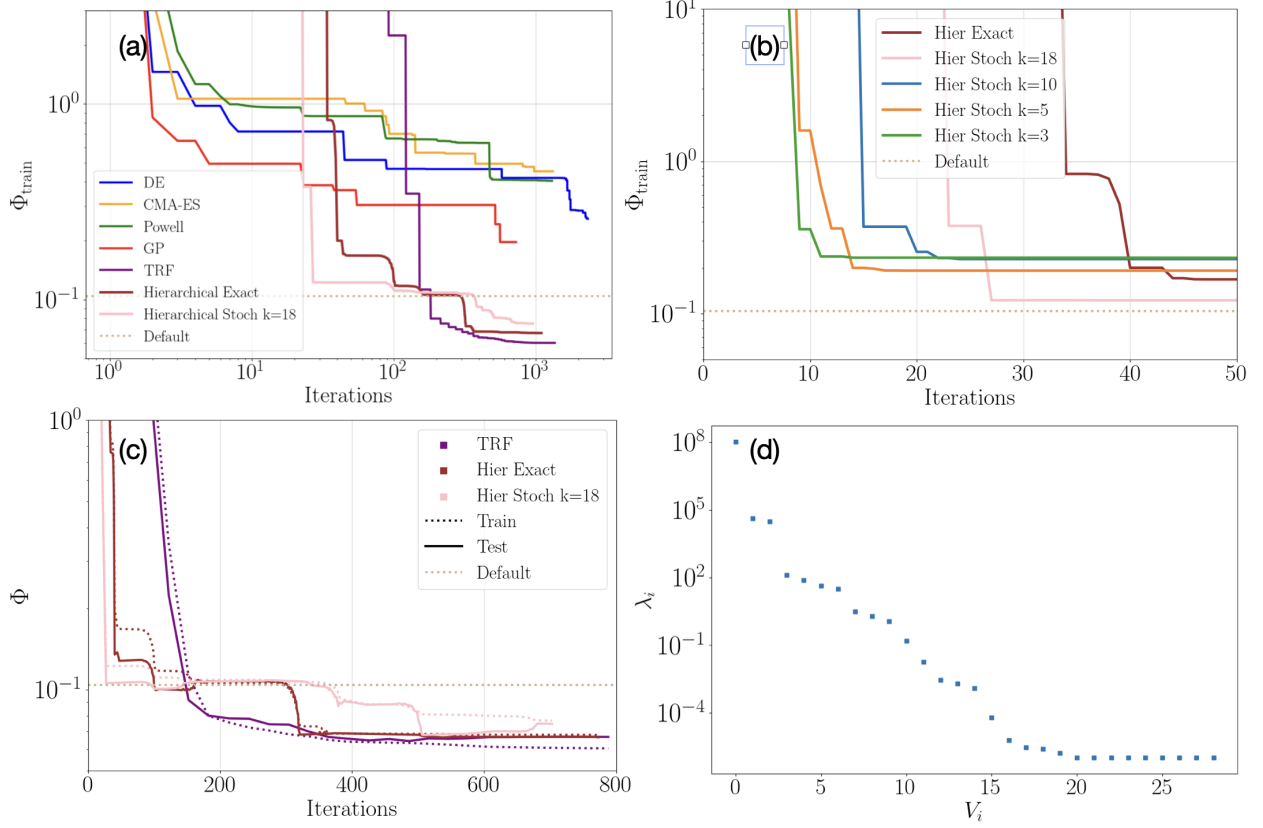


Figure 2: Optimization performance and geometric analysis. Figure (a) compares the convergence of the training loss (Φ_{train}) versus simulator iterations for the hierarchical methods (brown and pink) against the baseline algorithms, where the dotted line marks the default parameter loss. Figure (b) presents the sample efficiency in the early optimization phase (first 50 iterations) for the Hierarchical Stochastic strategy using varying subspace sizes k . Figure (c) displays the simultaneous evolution of the training loss (dotted lines) and test loss (solid lines) for the best-performing algorithms (Hierarchical and TRF). Figure (d) shows the eigenvalue spectrum ($\{\lambda_i\}$) of the Gauss-Newton Hessian, H_{GN} , as a function of the eigendirections V_i at the minimum θ_{final} found. The H_{GN} is represented as $H_{\text{GN}} = V \Lambda V^T$, with $\Lambda = \text{diag}(\lambda_1, \dots, \lambda_n)$. In this case, V_0 corresponds to the stiff subspace, while the remaining directions V_i are the sloppy subspace.

the training (80%) and test (20%) sets uniformly cover the experimental operating window, preventing the clustering of specific thermodynamic conditions in a single subset.

The global predictive capability of the optimized model is validated first in Figure 3(a), which presents a parity plot of the predicted versus experimental γ_O probabilities for all test set conditions across the five splits. The model achieves a global R^2 of 0.736, with consistent test loss values (Φ_{test}) across all splits (ranging from 0.054 to 0.087). This uniformity demonstrates that the algorithm has found a generalizable physical solution rather than overfitting to specific training subsets.

Figure 3(b) further details the model's performance by comparing simulations against experimental measurements for specific test conditions at varying pressures ($p = 0.4, 1.5, 3.0$ Torr). The optimized parameters (diamonds) yield a closer agreement with the experimental data (crosses) compared to the default parameters (squares), particularly in reproducing the temperature dependence of γ_O observed in the experiments. This improvement validates the hierarchical optimization approach as a robust tool for refining surface kinetics models in regimes where experimental data is sparse or noisy.

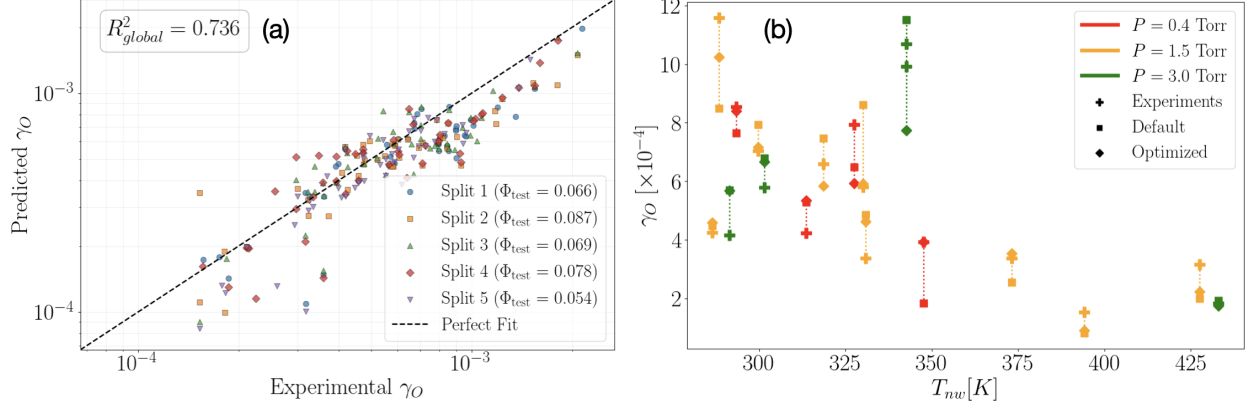


Figure 3: Validation of the optimized kinetics model. (a) Parity plot of predicted vs. experimental γ_O for the test sets of all 5 independent splits, showing a strong correlation ($R^2 = 0.736$). (b) Detailed comparison of γ_O as a function of wall temperature for selected test conditions at three different pressures, highlighting the accuracy gain of the optimized parameters (diamonds) over the default values (squares).

With the model's predictive power established, we examine the stability of the physical parameters themselves. Figure 4 summarizes the results, comparing the literature default parameters (green) with the median optimized values (orange) obtained across the five independent runs. The error bars represent the uncertainty quantified via the Hessian of the training loss calculated on the corresponding split at the median solution. The intervals are given by $\Delta\theta_i = \sqrt{2 \Delta\Phi \cdot (H_{GN}^{-1})_{ii}}$ [35], with a confidence interval threshold of $\Delta\Phi = 0.01 \times \Phi(\theta_{final})$.

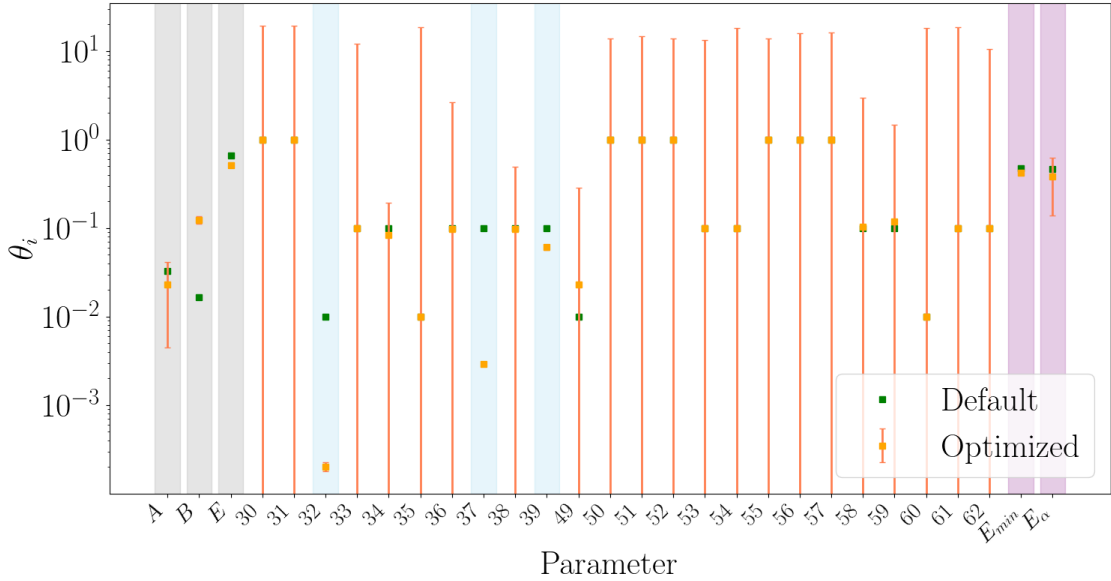


Figure 4: Comparison between the normalized default literature parameters (green) and the median optimized values (orange) obtained from 5-fold cross-validation. The numeric labels correspond to the steric factor indices (e.g., the number 30 corresponds to $k_{0,30}$, following the sequential reaction order of the full kinetic scheme). The error bars correspond to the Hessian-derived uncertainty bounds. Colored bars highlight the stiff parameters (Gray: Desorption; Blue: CO chemisorption; Pink: Metastable energies), while uncolored bars indicate sloppy parameters.

The magnitude of these error bars effectively maps the *stiffness* of the physical model: small bars indicate stiff parameters that are tightly constrained by the physics, while large bars reveal sloppy parameters where the model lacks sensitivity. As detailed in Table 1, the critical (stiff) parameters governing the system are identified as:

- The desorption frequencies of O_F , O_{2F} , and CO_F (parameters A , B , and E , highlighted in gray);
- The steric factors for the key CO chemisorption lifecycle reactions: its formation ($k_{0,32} : CO(g) + SV \longrightarrow CO_S$) and its recombination with atomic oxygen ($k_{0,37} : O(g) + CO_S \longrightarrow CO_2 + SV$ and $k_{0,39} : O_F + CO_S \longrightarrow CO_2(g) + SV$) (highlighted in blue);
- The characteristic energies for the creation and destruction of metastable states: E_α and E_{\min} (highlighted in pink).

Conversely, the steric factors for the remaining metastable rate coefficients and reactions involving physisorbed CO adsorption/desorption remain poorly constrained, as illustrated by the large uncolored error bars in Figure 4. This confirms that their broad uncertainties are a structural consequence of the model’s sloppiness rather than insufficient data.

Parameter	Default	Optimized (Median)
A	1.634×10^{-2}	1.158×10^{-2}
B	1.670×10^{-2}	1.245×10^{-3}
E [kJ/mol]	19.75	15.27
$k_{0,32}$	10^{-2}	2.9×10^{-3}
$k_{0,37}$	10^{-1}	2.2×10^{-3}
$k_{0,39}$	10^{-1}	6.1×10^{-2}
E_{\min} [eV]	2.90	2.69
E_α [eV]	0.29	0.27

Table 1: Default and optimized values (median of 5 splits) for the stiff parameters.

5 Conclusion and Outlooks

This work presents a novel data-driven framework for the optimization of physical models, addressing the fundamental challenge of learning from sparse data in computationally expensive systems. By bridging the gap between physical modeling and Scientific Machine Learning, we depart from standard black-box optimization strategies to introduce a hierarchical procedure that actively exploits the intrinsic geometry of the parameter space.

Central to our approach is the recognition that many physical systems are sloppy: their behavior is dominated by a low-dimensional latent manifold rather than the full parameter set. We leverage this structure by decomposing the optimization into stiff and sloppy subspaces. This geometric strategy allows the algorithm to rapidly converge onto the low-energy manifold, the *valley floor*, before refining the parameters along the softer directions, effectively mitigating the severe ill-conditioning that paralyzes traditional baseline optimizers.

A key methodological contribution is the implementation of this strategy via a stochastic reduced Hessian. We demonstrated that this low-rank approximation functions effectively as a linear autoencoder for the local curvature, extracting the latent structure of the landscape using a constant number of evaluations proportional to the intrinsic dimension (k) rather than the full parameter count (n). This property ensures the method scales favorably for high-dimensional problems and remains robust in low-data regimes.

We validated this framework by applying it to the refinement of mesoscopic surface kinetic schemes, which are essential for describing plasma-surface interactions. Specifically, we addressed the interaction of O_2 and CO_2 glow discharges with Pyrex reactor walls, utilizing a comprehensive dataset of 225 steady-state experimental conditions. Beyond optimization, we utilized the Hessian to derive data-driven uncertainty estimates. This analysis quantitatively confirmed that parameters related to the desorption frequencies of oxygen and carbon monoxide, the steric factors controlling chemisorbed CO formation and oxidation, and the energies required to create and destroy metastable states are well-constrained by the experimental data. In contrast, the other parameters are less sensitive.

Future research will focus on two distinct directions. First, we aim to analyze the insights gained from this data-driven approach to explore the underlying physics of atomic oxygen recombination on Pyrex surfaces. Second, while the current work focused on robust interpolation within the observed operational space, investigating the model’s limits in extrapolation remains a compelling challenge.

The proposed framework offers a model-agnostic solution that maximizes information extraction by targeting the problem’s geometric stiffness. It effectively bridges the gap between high-dimensional physical complexity and the constraints of data scarcity. Consequently, this approach establishes a transferable methodology for addressing inverse problems, extending well beyond the specific context of plasma kinetics.

Acknowledgments

The authors gratefully acknowledge Tiago Dias, Ana Sofía Morillo Candás, and Olivier Guaitella for providing unpublished experimental measurements obtained at *Laboratoire de Physique des Plasmas*, which were used in the experimental dataset for this work.

Funding

This work was supported by the Portuguese FCT - Fundação para a Ciência e a Tecnologia, under project's references UID/50010/2023, UID/PRR/50010/2025 and LA/P/0061/2020. This work was further supported by the European Union under Horizon Europe project CANMILK (DOI:10.3030/101069491). PV acknowledges support by project CECIND/00025/2022 of FCT.

Data availability

The code used to produce the results and figures in this paper is publicly available on GitHub at <https://github.com/joseAf28/PlasmaDM>. The data supporting the findings of this study is available within the repository.

References

- [1] Bryan C. Daniels, Yan Jiun Chen, James P. Sethna, Ryan N. Gutenkunst, and Christopher R. Myers. Sloppiness, robustness, and evolvability in systems biology. *Current Opinion in Biotechnology*, 19(4):389–395, August 2008. Funding Information: We would like to thank Ben Machta and Mark Transtrum for their keen insights into sloppiness and their assistance in developing some of the arguments presented here. We acknowledge grants USDA-ARS 1907-21000-027-03, NSF DMR-0705167, and NSF DGE-0333366.
- [2] Mark K. Transtrum, Benjamin Machta, Kevin Brown, Bryan C. Daniels, Christopher R. Myers, and James P. Sethna. Sloppiness and emergent theories in physics, biology, and beyond, 2015.
- [3] U. Maas and S.B. Pope. Simplifying chemical kinetics: Intrinsic low-dimensional manifolds in composition space. *Combustion and Flame*, 88(3):239–264, 1992.
- [4] Mark K. Transtrum, Benjamin B. Machta, and James P. Sethna. Geometry of nonlinear least squares with applications to sloppy models and optimization. *Physical Review E*, 83(3), March 2011.
- [5] Lawrence Cayton. Algorithms for manifold learning. Technical Report CS2005-0840, University of California, San Diego, 2005. Department of Computer Science and Engineering.
- [6] Richard S. Sutton and Andrew G. Barto. *Reinforcement Learning: An Introduction*. The MIT Press, second edition, 2018.
- [7] Donald R. Jones, Matthias Schonlau, and William J. Welch. Efficient global optimization of expensive black-box functions. *Journal of Global Optimization* 13: 455–492, 13:455–492, 1998.
- [8] Nikolaus Hansen. The CMA evolution strategy: A tutorial, 2023. arXiv:1604.00772.
- [9] Antonio Tejero-del Caz, Vasco Guerra, Duarte Gonçalves, Mário Lino da Silva, Luís Marques, Nuno Pinhão, Carlos D. Pintassilgo, and Luís L. Alves. The LisbOn KInetics Boltzmann solver. *Plasma Sources Science and Technology*, 28(4):043001, apr 2019.
- [10] George Karniadakis, Yannis Kevrekidis, Lu Lu, Paris Perdikaris, Sifan Wang, and Liu Yang. Physics-informed machine learning. *Nature Reviews Physics*, pages 1–19, 05 2021.
- [11] Geoffrey E Hinton and Ruslan R Salakhutdinov. Reducing the dimensionality of data with neural networks. *Science*, 313(5786):504–507, 2006.
- [12] Mark K. Transtrum, Benjamin B. Machta, and James P. Sethna. Why are nonlinear fits to data so challenging? *Physical Review Letters*, 104(6), February 2010.
- [13] Michael A. Lieberman and Allan J. Lichtenberg. *Principles of Plasma Discharges and Materials Processing*. John Wiley & Sons, 2nd edition, 2005.
- [14] Abhinash Kumar Singh, Jasminka Palo, Johanna Kihlman, Tiina Heikola, Mika Suvanto, Pekka Simell, and Niko M. Kinnunen. Non-thermal plasma assisted methane oxidation inside a dbd reactor: Effect of monometallic catalyst on energy efficiency and CO₂ selectivity. *Chemical Engineering Journal*, 521:166610, 2025.

[15] Gianfranco Federici, C.H. Skinner, J.N. Brooks, J.P. Coad, C. Grisolia, A.A. Haasz, Ahmed Hassanein, Volker Philipps, Charles Pitcher, J. Roth, W.R. Wampler, and D.G. Whyte. Plasma-material interactions in current tokamaks and their implications for next step fusion reactors. *Nuclear Fusion*, 41:1967, 05 2002.

[16] Vasco Guerra. Analytical model of heterogeneous atomic recombination on silicalike surfaces. *IEEE Transactions on Plasma Science*, 2007.

[17] José Afonso, Luca Vialeto, Vasco Guerra, and Pedro Viegas. Plasma-induced reversible surface modification and its impact on oxygen heterogeneous recombination. *Journal of Physics D: Applied Physics*, 57(4):04LT01, oct 2023.

[18] Pedro Viegas, Jorge Silveira, Tiago Cunha Dias, Olivier Guaitella, Ana Sofía Morillo Candás, and Vasco Guerra. Surface recombination in pyrex in oxygen DC glow discharges: mesoscopic modelling and comparison with experiments. *Plasma Sources Science and Technology*, 33(5):055003, may 2024.

[19] Jorge Nuno Machado Silveira. Plasma-surface interactions in plasmas for CO₂ conversion. Master's thesis, Instituto Superior Técnico - Universidade de Lisboa, December 2023. <https://scholar.tecnico.ulisboa.pt/records/7XCJfV5IdqyrXGp98L3YstNxAJzkiIFpxAEA?lang=en>.

[20] Blandine Berdugo. Surface recombination on pyrex in CO₂ glow discharges. Master's thesis, Université Paris-Saclay, 2024.

[21] Rainer Storn and Kenneth Price. Differential evolution – a simple and efficient heuristic for global optimization over continuous spaces. *Journal of Global Optimization*, 11:341–359, 1997.

[22] Nikolaus Hansen and Andreas Ostermeier. Completely derandomized self-adaptation in evolution strategies. *Evolutionary Computation*, 9(2):159–195, 2001.

[23] Mary Branch, Thomas Coleman, and Yuying li. A subspace, interior, and conjugate gradient method for large-scale bound-constrained minimization problems. *SIAM Journal on Scientific Computing*, 21:1–23, 07 2006.

[24] Michael J.D. Powell. An efficient method for finding the minimum of a function of several variables without calculating derivatives. *The Computer Journal*, 7(2):155–162, 1964.

[25] Carl Edward Rasmussen and Christopher K. I. Williams. *Gaussian Processes for Machine Learning*. The MIT Press, 2006.

[26] Jorge J Moré. The levenberg-marquardt algorithm: implementation and theory. In *Numerical Analysis*, volume 630 of *Lecture Notes in Mathematics*, pages 105–116. Springer, 1978.

[27] Mark K. Transtrum and James P. Sethna. Geodesic acceleration and the small-curvature approximation for nonlinear least squares, 2012. arXiv:1207.4999.

[28] Mark K. Transtrum, Bryan B. Machta, and James P. Sethna. An efficient, geometrically motivated algorithm for fitting sloppy models. *Physical Review E*, 83(3):036701, 2011.

[29] Jorge Nocedal and Stephen J. Wright. *Numerical Optimization*. Springer New York, NY, 2nd edition, 2006.

[30] Alaa Tharwat. Principal component analysis - a tutorial. *International Journal of Applied Pattern Recognition*, 3:197, 01 2016.

[31] Nathan Halko, Per-Gunnar Martinsson, and Joel A. Tropp. Finding structure with randomness: Probabilistic algorithms for constructing approximate matrix decompositions, 2010.

[32] Roger A. Horn and Charles R. Johnson. *Matrix Analysis*. Cambridge University Press, 2 edition, 2012.

[33] Barak A. Pearlmutter. Fast exact multiplication by the hessian. *Neural Computation*, 6(1):147–160, 01 1994.

[34] Ana-Sofia Morillo-Candas. *Investigation of fundamental mechanisms of CO₂ plasmas*. Theses, Université Paris Saclay (COMUE), December 2019. <https://polytechnique.hal.science/tel-03014566v1>.

[35] Alexander G. Kalmikov and Patrick Heimbach. A hessian-based method for uncertainty quantification in global ocean state estimation. *SIAM Journal on Scientific Computing*, 36(5):S267–S295, 2014.

[36] Swagatam Das and Ponnuthurai Nagaratnam Suganthan. Differential evolution: A survey of the state-of-the-art. *IEEE Transactions on Evolutionary Computation*, 15(1):4–31, 2011.

[37] Jorge Nocedal. Updating quasi-newton matrices with limited storage. *Mathematics of Computation*, 35(151):773–782, 1980.

[38] John A. Nelder and Roger Mead. A simplex method for function minimization. *The Computer Journal*, 7(4):308–313, 1965.

[39] Zsolt Ugray, Leon Lasdon, John Plummer, Fred Glover, James Kelly, and Rafael Martí. Scatter search and local nlp solvers: A multistart framework for global optimization. *INFORMS Journal on Computing*, 19(3):328–340, 2007.

[40] Adam Paszke, Sam Gross, Francisco Massa, Adam Lerer, James Bradbury, Gregory Chanan, Trevor Killeen, Zeming Lin, Natalia Gimelshein, Luca Antiga, et al. Pytorch: An imperative style, high-performance deep learning library. In *Advances in Neural Information Processing Systems 32*, pages 8026–8037. Curran Associates, Inc., 2019.

[41] Richard H. Byrd, Peihuang Lu, Jorge Nocedal, and Ciyou Zhu. A limited memory algorithm for bound constrained optimization. *SIAM Journal on Scientific Computing*, 16(5):1190–1208, 1995.

[42] Rajesh Shrestha. Natural gradient methods: Perspectives, efficient-scalable approximations, and analysis, 2023. arXiv:2303.05473.

[43] David Freeborn. Sloppy models, renormalization group realism, and the success of science. *Erkenntnis*, 90:645–673, 08 2025.

[44] Michael J. Evans and Jeffrey S. Rosenthal. *Probability and Statistics: The Science of Uncertainty*. W. H. Freeman and Company, New York, 2nd edition, 2010.

[45] Pauli Virtanen, Ralf Gommers, Travis E. Oliphant, Matt Haberland, Tyler Reddy, David Cournapeau, Evgeni Burovski, Pearu Peterson, Warren Weckesser, Jonathan Bright, Stéfan J. van der Walt, Matthew Brett, Joshua Wilson, K. Jarrod Millman, Nikolay Mayorov, Andrew R. J. Nelson, Eric Jones, Robert Kern, Eric Larson, C J Carey, İlhan Polat, Yu Feng, Eric W. Moore, Jake VanderPlas, Denis Laxalde, Josef Perktold, Robert Cimrman, Ian Henriksen, E. A. Quintero, Charles R. Harris, Anne M. Archibald, António H. Ribeiro, Fabian Pedregosa, Paul van Mulbregt, Aditya Vijaykumar, Alessandro Pietro Bardelli, Alex Rothberg, Andreas Hilboll, Andreas Kloeckner, Anthony Scopatz, Antony Lee, Ariel Rokem, C. Nathan Woods, Chad Fulton, Charles Masson, Christian Häggström, Clark Fitzgerald, David A. Nicholson, David R. Hagen, Dmitrii V. Pasechnik, Emanuele Olivetti, Eric Martin, Eric Wieser, Fabrice Silva, Felix Lenders, Florian Wilhelm, G. Young, Gavin A. Price, Gert-Ludwig Ingold, Gregory E. Allen, Gregory R. Lee, Hervé Audren, Irvin Probst, Jörg P. Dietrich, Jacob Silterra, James T Webber, Janko Slavić, Joel Nothman, Johannes Buchner, Johannes Kulick, Johannes L. Schönberger, José Vinícius de Miranda Cardoso, Joscha Reimer, Joseph Harrington, Juan Luis Cano Rodríguez, Juan Nunez-Iglesias, Justin Kuczynski, Kevin Tritz, Martin Thoma, Matthew Newville, Matthias Kümmeler, Maximilian Bolingbroke, Michael Tartre, Mikhail Pak, Nathaniel J. Smith, Nikolai Nowaczyk, Nikolay Shebanov, Oleksandr Pavlyk, Per A. Brodtkorb, Perry Lee, Robert T. McGibbon, Roman Feldbauer, Sam Lewis, Sam Tygier, Scott Sievert, Sebastiano Vigna, Stefan Peterson, Surhud More, Tadeusz Pudlik, Takuya Oshima, Thomas J. Pingel, Thomas P. Robitaille, Thomas Spura, Thouis R. Jones, Tim Cera, Tim Leslie, Tiziano Zito, Tom Krauss, Utkarsh Upadhyay, Yaroslav O. Halchenko, and Yoshiki Vázquez-Baeza. Scipy 1.0: fundamental algorithms for scientific computing in python. *Nature Methods*, 17(3):261–272, February 2020.

[46] Valery Kovalev, Natalia Afonina, and Valery Gromov. Heat transfer modelling to catalytic protection systems of space vehicles entering into martian atmosphere. In Z. Jiang, editor, *Shock Waves*, pages 597–602, Berlin, Heidelberg, 2005. Springer Berlin Heidelberg.

[47] Valery Kovalev and Anatoly Kolesnikov. Experimental and theoretical simulation of heterogeneous catalysis in aerothermochemistry (a review). *Fluid Dynamics*, 40:669–693, 09 2005.

[48] Anne Bourdon and Arnaud Bultel. Numerical simulation of stagnation line nonequilibrium airflows for reentry applications. *Journal of Thermophysics and Heat Transfer*, 227:168–177, 04 2008.

[49] Richard Aster, Brian Borchers, and Clifford Thurber. Parameter estimation and inverse problems. *Recherche*, 67:02, 01 2012.

[50] The scikit-optimize development team. scikit-optimize. <https://github.com/scikit-optimize/scikit-optimize>, 2016.

[51] Richard Lowe and Alison Tomlin. Low-dimensional manifolds and reduced chemical models for tropospheric chemistry simulations. *Atmospheric Environment*, 34(15):2425–2436, 2000.

Appendix

A Observed-data likelihood derivation

Here, we present the detailed derivation of the objective loss function based on a latent variable model. We assume the system is governed by an unobserved (latent) true state x^* , which is deterministically predicted by the model

parameters θ . The observables, $M = \{\tilde{M}, x^{\text{exp}}\}$, are treated as noisy measurements conditioned on this latent state. The observables are divided into two groups based on their dependencies:

- \tilde{M} represents measurements that are function of both the latent state x^* and the hyperparameters θ directly (such as the recombination probability)
- x^{exp} represents measurements that depend only on the latent space (such as surface or gas phase densities).

In the specific case of the physical system studied, the macroscopic observable corresponds to the recombination probability, γ_O , which is of the type \tilde{M} . This indicates that for this physical application $M = \{\gamma_O\}$.

A.1 Likelihood Formulation

The joint likelihood of the observed data for a single experiment is obtained by marginalizing over the latent state x^* :

$$p(\tilde{M}, x^{\text{exp}} | \theta) = \int dx^* p(\tilde{M} | x^*, \theta) p(x^{\text{exp}} | x^*) p(x^* | \theta). \quad (15)$$

The core assumption is that the latent state is a deterministic function of the parameters, which we denote as $x(\theta)$. This is expressed as a Dirac delta distribution: $p(x^* | \theta) = \delta(x^* - x(\theta))$. Substituting this into Eq.(15) collapses the integral to:

$$p(\tilde{M}, x^{\text{exp}} | \theta) = p(\tilde{M} | x(\theta), \theta) p(x^{\text{exp}} | x(\theta)). \quad (16)$$

We assume that all measurements are corrupted by additive Gaussian noise, such that:

$$p(x^{\text{exp}} | x(\theta)) = \mathcal{N}(x^{\text{exp}} | x(\theta), \Sigma_x), \quad (17)$$

$$p(\tilde{M} | x(\theta), \theta) = \mathcal{N}(\tilde{M} | \tilde{M}(x(\theta), \theta), \Sigma_{\tilde{M}}), \quad (18)$$

where $\tilde{M}(x(\theta), \theta)$ is the model prediction for the macroscopic observables \tilde{M} , and Σ_x and $\Sigma_{\tilde{M}}$ are the covariance matrices.

A.2 Approximation for the Loss Function

The likelihood in Eq.(16) depends on the unobserved latent state $x(\theta)$. To create a loss function based only on the observed data x^{exp} , we linearize the model prediction $\tilde{M}(x(\theta), \theta)$ around x^{exp} :

$$\tilde{M}(x(\theta), \theta) \approx \tilde{M}(x^{\text{exp}}, \theta) + J_x^{(\tilde{M})}(\theta)(x(\theta) - x^{\text{exp}}), \quad (19)$$

where $J_x^{(\tilde{M})}(\theta)$ is the Jacobian of \tilde{M} with respect to x and $\delta x = x(\theta) - x^{\text{exp}}$. From our assumption for $p(x^{\text{exp}} | x(\theta))$, the random variable δx follows a Gaussian distribution with zero mean, $\mathbb{E}[\delta x] = 0$, and covariance Σ_x .

The distribution for \tilde{M} conditioned on the observed x^{exp} can now be approximated as a new Gaussian, $\tilde{p}(\tilde{M} | x^{\text{exp}}, \theta) = \mathcal{N}(\mu(\theta), \tilde{\Sigma}_{\tilde{M}}(\theta))$, whose mean and covariance parameters are given by:

$$\mu(\theta) = \tilde{M}(x^{\text{exp}}, \theta) + J_x^{(\tilde{M})}(\theta) \mathbb{E}[\delta x] = \tilde{M}(x^{\text{exp}}, \theta), \quad (20)$$

$$\tilde{\Sigma}_{\tilde{M}}(\theta) = \Sigma_{\tilde{M}} + J_x^{(\tilde{M})}(\theta) \text{Cov}(\delta x) J_x^{(\tilde{M})T}(\theta) = \Sigma_{\tilde{M}} + J_x^{(\tilde{M})}(\theta) \Sigma_x J_x^{(\tilde{M})T}(\theta). \quad (21)$$

The total negative log-likelihood for a dataset $\mathcal{D} = \{(x_i^{\text{exp}}, \tilde{M}_i)\}_{i=1}^D$ is the objective loss function $\mathcal{L}(\theta) = \sum_{i=1}^D \mathcal{L}_i(\theta)$. For a single data point, this is:

$$\begin{aligned} \mathcal{L}_i(\theta) &= -\log \tilde{p}(\tilde{M}_i | x_i^{\text{exp}}, \theta) - \log p(x_i^{\text{exp}} | x_i(\theta)) = \\ &= \frac{1}{2}(\tilde{M}_i - \mu_i(\theta))^T \tilde{\Sigma}_{\tilde{M},i}^{-1}(\theta) (\tilde{M}_i - \mu_i(\theta)) + \frac{1}{2} \log |2\pi \tilde{\Sigma}_{\tilde{M},i}(\theta)| \\ &\quad + \frac{1}{2}(x_i^{\text{exp}} - x_i(\theta))^T \Sigma_{x,i}^{-1}(x_i^{\text{exp}} - x_i(\theta)) + \frac{1}{2} \log |2\pi \Sigma_{x,i}|. \end{aligned} \quad (22)$$

A.3 Simplified Loss for Relative Errors

We can obtain a simpler, unweighted loss function under several assumptions:

1. The model output M is insensitive to x , so the Jacobian $J_x^{(\tilde{M})}(\theta) \approx 0$. This implies $\mu_i(\theta) \approx \tilde{M}(x_i^{\text{exp}}, \theta)$ and $\tilde{\Sigma}_{\tilde{M},i} \approx \Sigma_{\tilde{M},i}$.
2. The covariance matrices $\Sigma_{\tilde{M}}$ and Σ_x are diagonal and constant with respect to θ . This allows us to drop the $\log |\cdot|$ terms.
3. The measurement error is proportional to the measurement value. For the diagonal covariances, this means $\Sigma_{\tilde{M},ii} \propto (\tilde{M}_i^{\text{exp}})^2$ and $\Sigma_{x,ii} \propto (x_i^{\text{exp}})^2$.

Under these assumptions, and ignoring constant scaling factors, the loss simplifies to a sum of squared relative errors:

$$\Phi(\theta) = \frac{1}{2} \sum_{i=1}^D \left[\left\| \frac{\tilde{M}_i^{\text{exp}} - \tilde{M}(x_i^{\text{exp}}, \theta)}{\tilde{M}_i^{\text{exp}}} \right\|_2^2 + \left\| \frac{x_i^{\text{exp}} - x_i(\theta)}{x_i^{\text{exp}}} \right\|_2^2 \right], \quad (23)$$

where the division is element-wise and $\|\cdot\|_2$ is the l_2 -norm. Noting that $M = \{\tilde{M}, x^{\text{exp}}\}$ and unrolling the $\|\cdot\|_2^2$ into its explicit sum, we obtain Eq.(2).

B Optimizer Implementation Details

All optimizations were performed on parameters normalized to the unit interval $[0, 1]$.

B.1 Baseline Algorithms

- Differential Evolution (DE): We used `scipy.optimize.differential_evolution` [45] with `best1bin` strategy, `recombination`= 0.7, `tol`= 0.1, `polish`=True and `seed`=42. The population size and maximum generations were set to 15 and 90, respectively;
- CMA-ES: We used the `cma` library [8]. `CMAEvolutionStrategy` was initialized with $\sigma_0 = 1.0$, `maxiter`= 70, `tolx`= 10^{-6} , and a population size of $4 + 4 \cdot \log(n)$ (where n is the parameter dimension);
- Powell (Baseline): We optimized the full parameter space using only Powell's method via `scipy.optimize.minimize(method='Powell')` [45], with its default termination criteria
- GP Optimization: We also optimized the normalized parameter space using Gaussian Process Bayesian optimization via `skopt.gp_minimize` [50]. The search was initialized with 40 random points, seeded with the default parameters, and run for a total of 980 function evaluations.
- Trust Region Reflective (TRF): We used `scipy.optimize.least_squares` with `method='trf'` [45]. This bound-constrained trust-region algorithm was initialized at the default parameter values ('`x0`') and restricted to the $[0, 1]$ interval, with a maximum function evaluation budget ('`max_nfev`') set to match the imposed limit;

B.2 Hierarchical Optimization

Our main algorithm's components were implemented using `scipy.optimize.minimize` [45].

- Stiff subspace: It was performed using Powell's [24];
- Sloppy subspace: It used Nelder-Mead methods [38], a simplex-based direct search.

Constraint Handling: The `scipy` implementation of Powell and Nelder-Mead does not support the `bounds` argument. Rather than using a wrapper, we enforced non-negative constraints directly within the simulator by taking the absolute value of the parameters before evaluation. While effective in our study, we note that more sophisticated solvers that explicitly accept `bounds` could also be employed.

C Hierarchical Optimization Algorithm

Following the high-level description in Algorithm 1, we provide a detailed specification for each of the functions referenced therein.

Gauss-Newton Hessian Computation

Algorithm 1 Hierarchical Optimization

Require: Objective loss $\Phi(\cdot)$, initial guess $\theta^{(0)}$, max iters N_{\max} , stopping $\varepsilon_{\text{stop}}$, Strategy $\in \{\text{Exact}, \text{Reduced}\}$

```

1: // Initialize Geometry
2: if Strategy is Exact then
3:   Compute Hessian  $H_{\text{GN}}(\theta^{(0)})$  using Eq.(3)
4:    $V_s^{(0)}, V_l^{(0)} \leftarrow \text{eigendecompose}(H_{\text{GN}}(\theta^{(0)}))$ 
5: else // Reduced Hessian Proxy
6:   Generate random basis  $\Omega \in \mathbb{R}^{n \times k}$ 
7:   Compute reduced Hessian  $H_{\text{small}}(\theta^{(0)}, \Omega)$  using Eq.(6)
8:    $U_s, U_l \leftarrow \text{eigendecompose}(H_{\text{small}}); V_s^{(0)} \leftarrow \Omega U_s; V_l^{(0)} \leftarrow \Omega U_l$ 
9: end if
10:  $i \leftarrow 1, \psi^{(0)} \leftarrow 0$ 
11: while  $i < N_{\max}$  do
12:   // 1) Stiff-subspace solve

$$\phi^{(i)} \leftarrow \arg \min_{\phi} \Phi \left( \theta^{(i-1)} + V_s^{(i-1)} \phi + V_l^{(i-1)} \psi^{(i-1)} \right)$$

13:    $\theta^{(i')} \leftarrow \theta^{(i-1)} + V_s^{(i-1)} \phi^{(i)}$ 
14:   // 2) Sloppy Re-alignment (Optional)
15:   Compute  $Y_l \leftarrow (r(\theta^{(i')}) + h V_l^{(i-1)}) - r(\theta^{(i')})/h$ 
16:    $H_l \leftarrow Y_l^T Y_l; U_l \leftarrow \text{eigendecompose}(H_l)$ 
17:    $V_l'^{(i-1)} \leftarrow V_l^{(i-1)} U_l$ 
18:   // 3) Sloppy-subspace solve

$$\psi^{(i)} \leftarrow \arg \min_{\psi} \Phi \left( \theta^{(i')} + V_l'^{(i-1)} \psi \right)$$

19:   // 4) Update full parameter

$$\theta^{(i)} = \theta^{(i')} + V_\ell'^{(i-1)} \psi^{(i)}$$

20:   // 5) Update Geometry
21:   if Strategy is Exact then
22:     Compute  $H_{\text{GN}}(\theta^{(i)})$ ; update  $V_s^{(i)}, V_l^{(i)}$ 
23:   else // Reduced Proxy
24:     Sample new  $\Omega$ ; compute  $H_{\text{small}}(\theta^{(i)}, \Omega)$ 
25:      $U_s, U_l \leftarrow \text{eigendecompose}(H_{\text{small}})$ 
26:     Update  $V_s^{(i)} \leftarrow \Omega U_s; V_l^{(i)} \leftarrow \Omega U_l$ 
27:   end if
28:   // 6) Check stopping
29:   if criteria  $(V_s^{(i-1)}, V_s^{(i)}) < \varepsilon_{\text{stop}}$  then
30:     break
31:   end if
32:    $i \leftarrow i + 1$ 
33: end while
34: return  $\theta^{(i)}$ 

```

For the computation of the *Gauss-Newton* Hessian matrix (H_{GN}) Eq.(3), we use the forward finite difference approximation. Moreover, to ensure the matrix is well-conditioned, we apply *Tikhonov* regularization. Hence, we have:

$$H_{\text{GN}} \leftarrow H_{\text{GN}} + \lambda_{\text{reg}} I \quad (24)$$

where I is the identity matrix.

Stiff and Sloppy Subspace Decomposition

We perform an eigendecomposition of the regularized H_{GN} to identify the stiff and sloppy subspaces of the parameter space. We denote $\{\lambda_i\}_{i=1}^n$ as the eigenvalues sorted in descending order, ($\lambda_1 \geq \lambda_2 \geq \dots \geq \lambda_n > 0$), and, $\{v_i\}_{i=1}^n$, their corresponding eigenvectors.

The stiff subspace is defined as the space spanned by the k_s eigenvectors, which collectively capture a fraction γ of the total variance, in the style of Principal Component Analysis (PCA) [30]. As presented in Table 2, we consider $\gamma = 0.90$. k_s is formally defined as the smallest integer satisfying:

$$k_s = \min \left\{ k \in \{1, \dots, n\} \mid \sum_{i=1}^k \lambda_i \geq \gamma \sum_{i=1}^n \lambda_i \right\} \quad (25)$$

The remaining $n - k_s$ dimensions form the sloppy subspace.

Reduced Sloppy Subspace for Optimization

For our numerical optimization procedure, we further prune the sloppy subspace to improve sample efficiency. We only include sloppy directions whose eigenvalues are significant relative to the largest eigenvalue within the same subspace.

λ_{k_s+1} is the largest sloppy eigenvalue, which we assume always belongs to the reduced sloppy subspace. Furthermore, we consider that the remaining sloppy directions v_i are included in the reduced sloppy subspace only if their eigenvalue λ_i meets a relative threshold τ :

$$\lambda_i \geq \tau \cdot \lambda_{k_s+1} \quad \text{for } i \in \{k_s + 2, \dots, n\} \quad (26)$$

The total number of sloppy directions retained is given by $k_l + 1$, where k_l , is the number of eigenvalues satisfying Eq.(26).

Hyperparameters

The optimization algorithm terminates when the convergence criteria (described in Section 2.3.5) $\varepsilon_{\text{stop}}$ is met or after a maximum of N_{max} iterations. The specific hyperparameter values used for all results presented in this work are listed in Table 2.

Hyperparameter	Description	Value
N_{max}	Number maximum of iterations	50
$\varepsilon_{\text{stop}}$	Convergence tolerance	10^{-4}
λ_{reg}	Regularization strength	10^{-6}
γ	Stiff subspace variance threshold	0.90
τ	Reduced sloppy subspace threshold	10^{-4}

Table 2: Hyperparameter values used in Algorithm 1.

D Implicit Hessian Construction via Finite Differences

We seek to compute the reduced Hessian matrix $H_{\text{small}} \in \mathbb{R}^{k \times k}$ without explicitly forming the high-dimensional Hessian $H_{\text{GN}} \in \mathbb{R}^{n \times n}$ or the Jacobian $J \in \mathbb{R}^{m \times n}$. Recall that the reduced Hessian is the projection of the Gauss-Newton approximation onto the subspace spanned by the orthonormal basis $\Omega \in \mathbb{R}^{n \times k}$:

$$H_{\text{small}} = \Omega^T H_{\text{GN}} \Omega. \quad (27)$$

Substituting the Gauss-Newton approximation $H_{\text{GN}} = J^T J$, we obtain:

$$H_{\text{small}} = \Omega^T (J^T J) \Omega = (J \Omega)^T (J \Omega). \quad (28)$$

Let $Y = J \Omega \in \mathbb{R}^{m \times k}$. The i -th column of Y , denoted Y_i , is the product of the Jacobian matrix and the i -th basis vector Ω_i . By definition, this matrix-vector product $J \Omega_i$ represents the directional derivative of the residual vector $r(\theta)$ along the direction Ω_i .

We can approximate this directional derivative efficiently using a forward finite difference scheme [33]. For a small step size h , the Taylor expansion of the residual vector is:

$$r(\theta + h\Omega_i) \approx r(\theta) + J(h\Omega_i) = r(\theta) + hY_i. \quad (29)$$

Rearranging for Y_i , we get the computable approximation:

$$Y_i \approx \frac{r(\theta + h\Omega_i) - r(\theta)}{h}. \quad (30)$$

Thus, we construct the matrix Y column-by-column by performing k additional simulator evaluations (one for each basis vector in Ω). The reduced Hessian is then obtained efficiently via the matrix multiplication $H_{\text{small}} = Y^T Y$, avoiding the $O(n)$ cost of the full Jacobian.

E Probabilistic Justification for Random Subspaces

The validity of using a random subspace to find the stiffest direction relies on the sloppy spectral gap [4]. We assume the true Hessian has a dominant eigenvalue λ_1 (stiff) with eigenvector v_1 , and a set of smaller eigenvalues bounded by λ_{sloppy} .

We aim to maximize the Rayleigh Quotient $R_H(v) = (v^T H v) / (v^T v)$ within our random subspace S . Let $\tilde{v} \in S$ be a unit vector in our subspace. We can decompose \tilde{v} into a component aligned with the true stiff direction v_1 and a component orthogonal to it (in the sloppy space):

$$\tilde{v} = \cos(\theta)v_1 + \sin(\theta)v_{\text{sloppy}}, \quad (31)$$

where θ is the angle between the random vector \tilde{v} and the true stiff direction v_1 . The curvature energy captured by this vector is:

$$R_H(\tilde{v}) = \tilde{v}^T H \tilde{v} \approx \lambda_1 \cos^2(\theta) + \lambda_{\text{sloppy}} \sin^2(\theta). \quad (32)$$

To successfully identify the stiff direction, the energy projected from the stiff mode must dominate the background energy from the sloppy modes. That is, we require the *signal* ($\lambda_1 \cos^2 \theta$) to be greater than the *noise floor* (λ_{sloppy}):

$$\lambda_1 \cos^2(\theta) > \lambda_{\text{sloppy}} \iff \frac{\lambda_1}{\lambda_{\text{sloppy}}} > \frac{1}{\cos^2(\theta)}. \quad (33)$$

For a random subspace of rank k in a parameter space of dimension n , the expected squared overlap between a random vector and a fixed target vector is $\mathbb{E}[\cos^2(\theta)] = k/n$ [31]. Substituting this expectation yields the critical condition for success:

$$\frac{\lambda_1}{\lambda_{\text{sloppy}}} > \frac{n}{k}. \quad (34)$$

This inequality states that as long as the stiffness ratio ($\lambda_1/\lambda_{\text{sloppy}}$) exceeds the dimensionality ratio (n/k), the local energy landscape within the random subspace will be dominated by the projection of the true stiff direction [4]. This ensures that the eigenvector corresponding to the largest eigenvalue of H_{small} is a reliable proxy for v_1 .

F Derivation of the Upper Bound for $\|\nabla\Phi(\theta_{\text{final}})\|_2$

We start by assuming that the algorithm has successfully converged after N iterations. Hence, the stiff subspace stabilization criterion, ($V_s^{(N-1)} \approx V_s^{(N)}$) is fulfilled and we may conclude that $P_s^{(N)} \nabla\Phi(\theta_{\text{final}}) = 0$, with $P_s = V_s V_s^T$ and $P_l = V_l V_l^T$.

Moreover, since the projection operators form a complete basis ($P_s + P_l = I$), the final gradient must lie entirely in the sloppy subspace: $\nabla\Phi(\theta_{\text{final}}) = P_l \nabla\Phi(\theta_{\text{final}})$. We can write $\nabla\Phi(\theta_{\text{final}})$ in terms of the eigenbasis of H_{final} as

$$\nabla\Phi(\theta_{\text{final}}) = H_{\text{final}} \Delta\tilde{\theta}, \quad (35)$$

which is valid as H_{final} is a full-rank matrix, and $\Delta\tilde{\theta}$ corresponds to the needed displacement vector. The Hessian H_{final} in its eigenbasis is given by $H_{\text{final}} = \sum_i \lambda_i v_i v_i^T$. As a result, we can directly bound the norm of this vector as:

$$\|\nabla\Phi(\theta_{\text{final}})\|_2 = \|P_l H_{\text{final}} \Delta\tilde{\theta}\|_2 \leq \|P_l H_{\text{final}}\|_2 \cdot \|\Delta\tilde{\theta}\|_2. \quad (36)$$

The Hessian H_{final} in its eigenbasis is given by $H_{\text{final}} = \sum_i \lambda_i v_i v_i^T$, implying that

$$P_l H_{\text{final}} = \sum_{j \in \text{sloppy}} v_j v_j^T \sum_i \lambda_i v_i v_i^T = \sum_{j \in \text{sloppy}} \sum_i \lambda_i v_j (v_j^T v_i) v_i^T. \quad (37)$$

Due to the orthonormality of the eigenvectors ($v_j^T v_i = \delta_{ij}$), the expression simplifies to:

$$P_l H_{\text{final}} = \sum_{j \in \text{sloppy}} \lambda_j v_j v_j^T. \quad (38)$$

As a result, the spectral norm of $P_l H_{\text{final}}$ is given by:

$$\|P_l H_{\text{final}}\|_2 = \max_{j \in \text{sloppy}} |\lambda_j| = |\lambda_{\max \text{sloppy}}|. \quad (39)$$

Substituting back into inequality (36), we arrive at the following expression:

$$\|\nabla \Phi(\theta_{\text{final}})\|_2 \leq |\lambda_{\max \text{sloppy}}| \cdot \|\Delta \tilde{\theta}\|_2 \quad (40)$$

The bound depends on the constructed $\Delta \tilde{\theta}$. To provide a physically meaningful result, we must relate this to the true displacement from the local minimum, $\Delta \theta = \theta_{\text{final}} - \theta_{\min}$. The Taylor expansion around the local minimum provides the link:

$$\nabla \Phi(\theta_{\text{final}}) \approx H(\theta_{\min}) \Delta \theta. \quad (41)$$

By comparing this to Eq.(35), we see that $\Delta \tilde{\theta} = (H_{\text{final}})^{-1} H_{\min} \Delta \theta$. Assuming that θ_{final} is close to θ_{\min} , the Hessians are nearly identical ($H_{\text{final}} \approx H_{\min}$), justifying the approximation $\Delta \tilde{\theta} \approx \Delta \theta$.